ENSEMBLE MONTE CARLO SIMULATION OF THE 4.8μm DEEP WELL QUANTUM CASCADE LASERS

by

Yanbing Shi

A project report submitted in partial fulfillment of
the requirements for the degree of

Master of Science
(Electrical Engineering)

at the

UNIVERSITY OF WISCONSIN–MADISON

2010

1. Introduction of quantum cascade lasers

As early as 1971, the possibility of emission between confined subbands of semiconductor quantum wells has been proposed [1]. Adopting such idea, the first electrically pumped Quantum Cascade Laser (QCL) was experimentally demonstrated in 1994 [2]. The QCL is made by a periodic series of thin layers with different bandgaps to form a multiple-quantum-well structure. Each period containing several tens of layers is called a stage. Each stage contains an electron-injecting region (injector) and an active region where the optical emissions occur. Schematics of the bandstructure and the lasing process for two successive stages of a QCL under the applied bias are shown in Fig. 1.1. An electron injected into the left end, from the previous stage, first experience several transitions through non-radiative scatterings, and reaches the bottom of the miniband. Then it tunnels through a relatively thick barrier at the end of the injector to fill the upper lasing level 3 (the upper red line) localized in the active region. Due to the large optical coupling strength between the upper lasing level 3 and the lower lasing level 2, the electron has large chance to make a radiative transition (the yellow wavy lines) between the two levels, and consequently emits a photon. The electron in the lower lasing level 2 is quickly relaxed to level 1, which might be assisted by phonon emission. Finally, the electron tunnels to the injector in the next stage and triggers another photon emission. This process repeats in each stage.

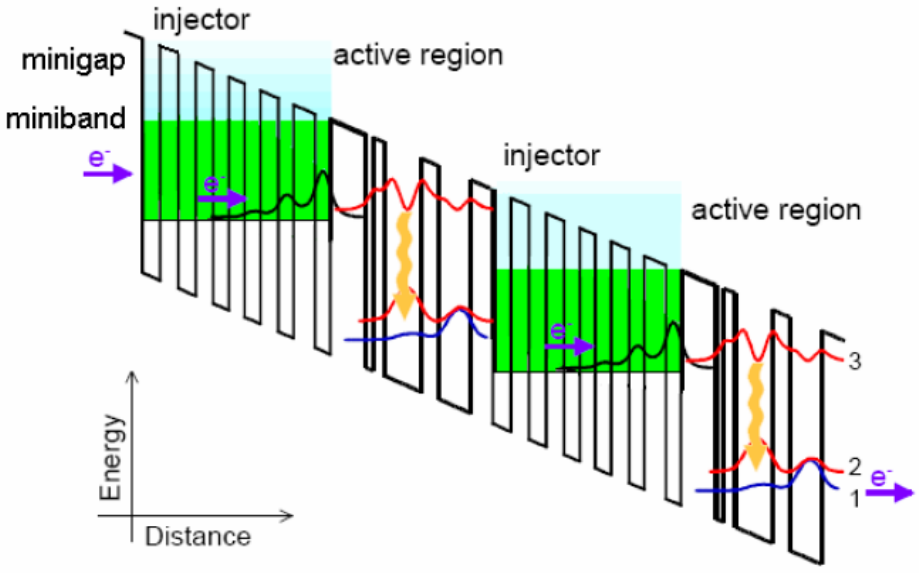

Fig. 1.1 Schematics of bandstructure and lasing process in a QCL

Owning to its intersubband nature of the optical transition as well as the cascading process, the QCL has several key advantages [3]. First, the emission wavelength primarily depends on the geometry of the structure, rather than the material bandgap. In other words, by appropriate designs, the QCL is able to achieve a wide range of lasing frequency using the well developed material system such as GaAs- or InP-based heterostructure. Second, multiple photon emission per electron is achieved thanks to the cascading feature, which significantly enhances the output optical power of the lasers.

Since the invention of the QCL, its optical performance has been greatly improved: the laser frequency has been expanded from mid-infrared [3, 4] to terahertz [5], and the continuous-wave operation has been achieved above the room temperature [6]. In addition, the QCL has been demonstrated on InAlAs/GaInAs [1], GaAs/AlGaAs [7], and Si/SiGe [8] material system. Three distinct designs of the active region, the so-called 'vertical' [9], 'diagonal' transition [10] as well as the 'superlattice' [11] active regions, have been proposed. Up to date, QCLs have been commercialized at the wafer, device, and system levels by over 15 companies [12].

In this report, we focus on the simulation of electron transport in QCLs. The numerical calculation of electronic states in QCLs by the **k·p** method and the effective mass equation is first introduced. Then the framework of the ensemble Monte Carlo (EMC) method for QCL simulation is presented. Finally, the simulation results of two specific mid-infrared QCLs – the well-developed 9.4 μm GaAs/AlGaAs QCL [13] is used to demonstrate the accuracy of the simulation; and then the simulation of the new developed 4.8 μm deep-well (DW) InAlAs/GaInAs QCL [14] supports the population inversion above the threshold as well as the effect of electron-electron scattering.

2. Electronic states

2.1 Γ-valley electronic states

In this section, the **k·p** method for solving the Γ valley states is briefly introduced, and is extended from bulk semiconductor to heterostructures.

A. Bulk semiconductor

For an electron in a bulk crystal, the Hamiltonian of the electron is

$$H_0 = \frac{p^2}{2m_0} + V_c(\vec{r}) \tag{2-1}$$

where $V_c(\vec{r})$ is the periodic crystal potential. By taking the spin-orbit interaction into account, the Hamiltonian near the zone center can be written as

$$H_{bulk} = H_0 + \frac{\hbar}{4m_0^2c^2}\left(\nabla V \times \vec{p}\right)\cdot\vec{\sigma} \tag{2-2}$$

where $\vec{\sigma}$ is the Pauli spin matrix with components

$$\overline{\overline{\sigma}}_x = \begin{bmatrix} 0 & 1 \\ 1 & 0 \end{bmatrix},\ \overline{\overline{\sigma}}_y = \begin{bmatrix} 0 & -i \\ i & 0 \end{bmatrix},\ \overline{\overline{\sigma}}_z = \begin{bmatrix} 1 & 0 \\ 0 & -1 \end{bmatrix}. \tag{2-3}$$

The time-independent Schrodinger equation becomes

$$\left[\frac{p^2}{2m_0} + V(\vec{r}) + \frac{\hbar}{4m_0^2c^2}\left(\nabla V \times \vec{p}\right)\cdot\vec{\sigma}\right]\psi_{n,\vec{k}}(\vec{r}) = E_n(k)\psi_{n,\vec{k}}(\vec{r}). \tag{2-4}$$

Based on Bloch's theorem, the solution of the wavefunction has the form of

$$\psi_{n,\vec{k}}(\vec{r}) = e^{i\vec{k}\cdot\vec{r}}u_{n,\vec{k}}(\vec{r}) \tag{2-5}$$

where $u_{n,\vec{k}}(\vec{r}) = u_{n,\vec{k}}(\vec{r}+\vec{R})$ is the periodic cell function. Therefore, the Schrodinger equation in terms of cell function can be derived as

$$\left[\frac{p^2}{2m_0} + V(\vec{r}) + \frac{\hbar}{m_0}\vec{k}\cdot\vec{p} + \frac{\hbar}{4m_0^2c^2}\left(\nabla V \times \vec{p}\right)\cdot\vec{\sigma} + \frac{\hbar^2}{4m_0^2c^2}\left(\nabla V \times \vec{k}\right)\cdot\vec{\sigma}\right]u_{n,\vec{k}}(\vec{r})$$

$$= \left[E_n(k) - \frac{\hbar^2k^2}{2m_0}\right]u_{n,\vec{k}}(\vec{r}). \tag{2-6}$$

The last term on the left-hand side is small compared with the other terms, since the

crystal momentum $\hbar\vec{k}$ is much smaller than the atomic momentum $\vec{p}$ in the far interior of the atom where most of the spin-orbit interaction occurs [15], which yields

$$\left[\frac{p^2}{2m_0}+V(\vec{r})+\frac{\hbar}{4m_0^2c^2}\left(\nabla V\times\vec{p}\right)\cdot\vec{\sigma}+\frac{\hbar}{m_0}\vec{k}\cdot\vec{p}\right]u_{n,\vec{k}}(\vec{r})=\left[E_n(k)-\frac{\hbar^2k^2}{2m_0}\right]u_{n,\vec{k}}(\vec{r})\cdot \quad (2\text{-}7)$$

The cell function $u_{n,\vec{k}}(\vec{r})$ can be expanded by the superposition of a complete set of basis function

$$u_{n,\vec{k}}(\vec{r})=\sum_j a_j u_{j0}(\vec{r}) \quad (2\text{-}8)$$

where the basis function $u_{j0}(\vec{r})=u_{j,\vec{k}=0}(\vec{r})$ is also the band-edge function with zero kinetic energy. Based on Luttinger-Kohn's model for degenerate bands [16], eight bands - the conduction (c), heavy-hole (hh), light-hole (lh), and spin-orbit split-off (so) bands, all doubly degenerate, are taken into account, and the eight basis functions $u_{j0}(\vec{r})$ are chosen as

$$\begin{aligned}
&|u_{10}\rangle=\left|iS\uparrow\right\rangle && |u_{50}\rangle=\left|iS\downarrow\right\rangle\\
&|u_{20}\rangle=-\frac{1}{\sqrt{2}}\left|(X+iY)\uparrow\right\rangle=\left|\frac{3}{2},\frac{3}{2}\right\rangle && |u_{60}\rangle=\frac{1}{\sqrt{2}}\left|(X-iY)\downarrow\right\rangle=\left|\frac{3}{2},-\frac{3}{2}\right\rangle\\
&|u_{30}\rangle=\frac{1}{\sqrt{6}}\left|-(X+iY)\downarrow+2Z\uparrow\right\rangle=\left|\frac{3}{2},\frac{1}{2}\right\rangle && |u_{70}\rangle=\frac{1}{\sqrt{6}}\left|(X-iY)\uparrow+2Z\downarrow\right\rangle=\left|\frac{3}{2},-\frac{1}{2}\right\rangle\\
&|u_{40}\rangle=\frac{1}{\sqrt{3}}\left|(X+iY)\downarrow+Z\uparrow\right\rangle=\left|\frac{1}{2},\frac{1}{2}\right\rangle && |u_{80}\rangle=\frac{1}{\sqrt{3}}\left|(X-iY)\uparrow-Z\downarrow\right\rangle=\left|\frac{1}{2},-\frac{1}{2}\right\rangle
\end{aligned} \quad (2\text{-}9)$$

Then apply the matrix formulation of the time-independent perturbation theory, the coefficients a_j for the basis functions can be evaluated by solving the eigenvalue problem

$$\sum_j H_{8\times8}^{ij}a_j=Ea_i \quad (2\text{-}10)$$

where j runs over total 8 bands, the matrix elements are calculated by $H_{8\times8}^{ij}=\left\langle u_{i0}\left|H_{bulk}\right|u_{j0}\right\rangle$. If the strain effects on band structures are also included [17], the 8×8 Hamiltonian matrix can be expressed as [18, 19]

$$\overline{\overline{H}}_{8\times 8}=\begin{bmatrix} E_C+A & -\sqrt{3}V & \sqrt{2}U & U & 0 & 0 & V^* & \sqrt{2}V^* \\ -\sqrt{3}V^* & E_V-P-Q & S & \frac{1}{\sqrt{2}}S & 0 & 0 & -R & -\sqrt{2}R \\ \sqrt{2}U & S^* & E_V-P+Q & \sqrt{2}Q & -V^* & -R & 0 & -\sqrt{\frac{3}{2}}S \\ U & \frac{1}{\sqrt{2}}S^* & \sqrt{2}Q & E_V-P-\Delta & \sqrt{2}V^* & \sqrt{2}R & -\sqrt{\frac{3}{2}}S & 0 \\ 0 & 0 & -V & \sqrt{2}V & E_C+A & \sqrt{3}V^* & \sqrt{2}U & -U \\ 0 & 0 & -R^* & \sqrt{2}R^* & \sqrt{3}V & E_V-P-Q & -S^* & \frac{1}{\sqrt{2}}S^* \\ V & -R^* & 0 & -\sqrt{\frac{3}{2}}S^* & \sqrt{2}U & -S & E_V-P+Q & -\sqrt{2}Q \\ \sqrt{2}V & -\sqrt{2}R^* & -\sqrt{\frac{3}{2}}S^* & 0 & -U & \frac{1}{\sqrt{2}}S & -\sqrt{2}Q & E_V-P-\Delta \end{bmatrix} \tag{2-11}$$

$$A=A_k+A_\varepsilon,\quad P=P_k+P_\varepsilon,\quad Q=Q_k+Q_\varepsilon \tag{2-12}$$

$$A_k=\frac{\hbar^2}{2m_e^*}\left(k_x^2+k_y^2+k_z^2\right),\quad A_\varepsilon=a_c(\varepsilon_{xx}+\varepsilon_{yy}+\varepsilon_{zz}) \tag{2-13}$$

$$P_k=\frac{\hbar^2\gamma_1}{2m_0}\left(k_x^2+k_y^2+k_z^2\right),\quad P_\varepsilon=-a_v(\varepsilon_{xx}+\varepsilon_{yy}+\varepsilon_{zz}) \tag{2-14}$$

$$Q_k=\frac{\hbar^2\gamma_2}{2m_0}\left(k_x^2+k_y^2-2k_z^2\right),\quad Q_\varepsilon=-\frac{b}{2}(\varepsilon_{xx}+\varepsilon_{yy}+\varepsilon_{zz}) \tag{2-15}$$

$$V=\frac{1}{\sqrt{6}}P_{cv}\left(k_x+ik_y\right) \tag{2-16}$$

$$U=\frac{1}{\sqrt{3}}P_{cv}k_z \tag{2-17}$$

$$P_{cv}=\frac{\hbar}{m_0}\left\langle iS\left|\frac{\hbar}{i}\frac{\partial}{\partial x}\right|X\right\rangle \tag{2-18}$$

$$R=\frac{\hbar^2}{2m_0}\sqrt{3}\left[-\gamma_2\left(k_x^2-k_y^2\right)+2i\gamma_3k_xk_y\right] \tag{2-19}$$

$$S=\frac{\hbar^2\gamma_3}{2m_0}2\sqrt{3}\left(k_x-ik_y\right)k_z \tag{2-20}$$

E_C and E_V are the unstrained conduction- and valence-band edges, respectively;

Δ is the spin-orbit split-off energy. m_e^* is the electron effective mass; a_c, a_v and b are the Bir-Pikus deformation potentials [17]; P_{cv} is the interband momentum matrix element defined by Kane [20]; γ_1, γ_2 and γ_3 are the modified Luttinger parameters [21]

$$\gamma_1 = \gamma_1^L - \frac{E_P}{3E_g}, \quad \gamma_2 = \gamma_2^L - \frac{E_P}{6E_g}, \quad \gamma_3 = \gamma_3^L - \frac{E_P}{6E_g} \tag{2-21}$$

where γ_1^L, γ_2^L and γ_3^L are the standard Luttinger parameters [16]; E_g is the energy gap; and $E_P = 2m_0 P_{cv}^2 / \hbar^2$ is the energy parameter for P_{cv}. The strain tensor components ε_{xx}, ε_{yy}, and ε_{zz} are [15]

$$\varepsilon_{xx} = \varepsilon_{yy} = \frac{a_0 - a}{a}, \quad \varepsilon_{zz} = -\frac{2C_{12}}{C_{11}}\varepsilon_{xx}, \quad \varepsilon_{xy} = \varepsilon_{yz} = \varepsilon_{zx} = 0 \tag{2-22}$$

where a_0 and a are the lattice constants of the substrate and the layer material, and C_{11} and C_{12} are the elastic stiffness constants. The material parameters used in the **k·p** method are summarized in Ref. [22].

In sum, the eigenvalues of the 8×8 Hamiltonian matrix give the energies E_n of the conduction, heavy-hole, light-hole, and spin-orbit split-off bands, and the corresponding wavefunctions can be obtained from the eigenvectors $\{a_j\}$ by

$$\psi_{n,\vec{k}}(\vec{r}) = e^{i\vec{k}\cdot\vec{r}} \sum_j a_j u_{j0}(\vec{r}) \tag{2-23}$$

B. Heterostructures

Quantum cascade lasers are made by the growth of a set of atomically abrupt (typically several nanometers) layers composed of materials with different bandgaps to form multiple quantum wells and barriers. Due to the sharp band discontinuity at each heterojunction, electron motion is confined in *z* direction, the growth direction. Thus its energy is quantized, and a set of subbands is formed. The Hamiltonian of the electron in a heterostructure system under the biased electric field *F* along *z* direction can be expressed as

$$H = H_{bulk} + U(z) \tag{2-24}$$

$$U(z) = V_B(z) - |e| Fz - |e| \varphi(z) \tag{2-25}$$

where $U(z)$ is the perturbed potential including the potential of quantum wells and barriers $V_B(z)$, and the term $-|e| Fz - |e| \varphi(z)$ owing to external field and the specific distribution of free electrons in the linear potential drop approximation.

The **k·p** method in the envelope function approximation expands the wavefunction on the cell functions as [18]

$$\psi_{n,\vec{k}_{\|}}(\vec{r}) = \sum_j F^j_{n,\vec{k}_{\|}}(\vec{r}) u_{j0}(\vec{r}) \tag{2-26}$$

$$F^j_{n,\vec{k}_{\|}}(\vec{r}) = \frac{e^{i\vec{k}_{\|}\cdot\vec{r}_{\|}}}{\sqrt{A}} g_{n,j}(z) u_{j0}(\vec{r}) \tag{2-27}$$

where $g_{n,j}(z)$ are the envelope functions that slowly vary over the unit cells, and n here is the index of the energy subband, which can be either the conduction or the valance (hh, lh or so) bands; $\vec{k}_{\|} = \vec{k}_x + \vec{k}_y$ is the in-plane wavevector. Substitute this specified wavefunction $\psi_{n,\vec{k}_{\|}}(\vec{r})$ along with the perturbed Hamiltonian H into the Schrodinger equation, which yields the eigenvalue problem

$$\sum_j \left[H^{ij}_{8\times 8}\left(\vec{k}_{\|}, \vec{k}_z = -i\frac{\partial}{\partial z} \right) + U(z)\delta_{ij} \right] g_{n,j}(z) = E_n g_{n,i}(z) \tag{2-28}$$

where is δ_{ij} the Kronecker delta. Since for the typical operation condition of QCLs, most electrons occupy the states near subband bottoms, we first simplify the 8-band Hamiltonian matrix by substituting $k_x = k_y = 0$ into (2-11), which yields

$$\overline{\overline{H}}_{8\times 8} = \begin{bmatrix} \overline{\overline{H}}^{U}_{4\times 4} & 0 \\ 0 & \overline{\overline{H}}^{L}_{4\times 4} \end{bmatrix} \tag{2-29}$$

where the two decoupled sub-matrices are

$$\overline{\overline{H}}^{U}_{4\times 4} = \begin{bmatrix} E_C + \frac{m_0}{m_e^*}E_z + A_\varepsilon & 0 & \sqrt{\frac{2}{3}E_P E_z} & \sqrt{\frac{1}{3}E_P E_z} \\ 0 & E_V - (\gamma_1 - 2\gamma_2)E_z - P - Q_\varepsilon & 0 & 0 \\ \sqrt{\frac{2}{3}E_P E_z} & 0 & E_V - (\gamma_1 + 2\gamma_2)E_z - P_\varepsilon + Q_\varepsilon & -2\sqrt{2}\gamma_2 E_z + Q_\varepsilon \\ \sqrt{\frac{1}{3}E_P E_z} & 0 & -2\sqrt{2}\gamma_2 E_z + Q_\varepsilon & E_V - \Delta - \gamma_1 E_z - P_\varepsilon \end{bmatrix}$$

(2-30)

$$\overline{\overline{H}}^{L}_{4\times4}=\begin{bmatrix} E_C+\frac{m_0}{m_e^*}E_z+A_\varepsilon & 0 & \sqrt{\frac{2}{3}E_PE_z} & -\sqrt{\frac{1}{3}E_PE_z} \\ 0 & E_V-(\gamma_1-2\gamma_2)E_z-P-Q_\varepsilon & 0 & 0 \\ \sqrt{\frac{2}{3}E_PE_z} & 0 & E_V-(\gamma_1+2\gamma_2)E_z-P_\varepsilon+Q_\varepsilon & 2\sqrt{2}\gamma_2E_z-Q_\varepsilon \\ -\sqrt{\frac{1}{3}E_PE_z} & 0 & 2\sqrt{2}\gamma_2E_z-Q_\varepsilon & E_V-\Delta-\gamma_1E_z-P_\varepsilon \end{bmatrix} \tag{2-31}$$

where $E_z=\hbar^2k_z^2/2m_0$. The eigenvalues of each sub-matrix are identical, and if we neglect the variation of $u_{j0}(\vec{r})$ within a small lattice unit cell, and are only interested in the variation of $g_{n,j}(z)$ extended in multiple layers, the eigenvalue problem of $\overline{\overline{H}}_{8\times8}$ is reduced to solving either $\overline{\overline{H}}^{U}_{4\times4}$ or $\overline{\overline{H}}^{L}_{4\times4}$. Moreover, in this approximation the off-diagonal terms in the second row and column in either sub-matrix are all zero, which means the heavy-hole band is decoupled with the other bands. Since we are only interested in the conduction band where the electron transport, the sub-matrix can be further reduced to

$$\overline{\overline{H}}_{3\times3}=\begin{bmatrix} E_c+(1+2F_K)E_z+A_\varepsilon & \sqrt{\frac{2}{3}E_PE_z} & \sqrt{\frac{1}{3}E_PE_z} \\ \sqrt{\frac{2}{3}E_PE_z} & E_v-(\gamma_1+2\gamma_2)E_z-P_\varepsilon+Q_\varepsilon & -2\sqrt{2}\gamma_2E_z+\sqrt{2}Q_\varepsilon \\ \sqrt{\frac{1}{3}E_PE_z} & -2\sqrt{2}\gamma_2E_z+\sqrt{2}Q_\varepsilon & E_v-\Delta_{so}-\gamma_1E_z+P_\varepsilon \end{bmatrix} \tag{2-32}$$

where F_K represents the contribution of higher conduction bands to the effective mass of the Γ_6 conduction-band electrons [20], and satisfies

$$\frac{1}{m_e^*}=\frac{2F_K}{m_0}+\frac{1}{m_0}. \tag{2-33}$$

Then (2-28) is reduced to

$$\sum_j\left[H^{ij}_{3\times3}\left(\bar{k}_z=-i\frac{\partial}{\partial z}\right)+U(z)\delta_{ij}\right]g_{n,j}(z)=E_ng_{n,i}(z) \tag{2-34}$$

where *j* only runs over three bands (c, lh, so).

To solve the coupled differential equations (2-34), the reciprocal-space numerical technique [23, 24] relying on the periodicity of the QCL structure along z direction is employed. In this approach, the envelope function $g_{n,j}(z)$ is expanded in a Fourier series [24]

$$g_{n,j}(z) = \sum_{m=-N_G}^{+N_G} a_{mn}^{j} e^{iG_m z} \tag{2-35}$$

where $G_m = 2m\pi / d \quad (m = 0, \pm 1, \cdots, \pm N_G)$ are the reciprocal vectors corresponding to the length of each periodic unit *d* in the QCL structure, and *d* can be chosen as the length of integer stages (usually 2 stages in the simulation). Substituting this expression into (2-34), multiplying both sides by $e^{-iG_{m'}z}$, and integrating over *d*, then the coupled differential equations are equivalent to the eigenvalue problem of a $3(2N_G+1)\times 3(2N_G+1)$ super matrix

$$\sum_{j,m'}\sum_{j',m} a_{mn}^{j'} \frac{1}{d}\int_0^d dz e^{i(G_m - G_{m'})}\left[H_{3\times 3}^{jj'}(k_z = G_m) + U(z)\delta_{jj'} \right] = E_n a_{m'n}^{j} \tag{2-36}$$

$$\text{or} \quad \begin{bmatrix} \widetilde{H}_{(-N_G)(-N_G)} & \cdots & \widetilde{H}_{(-N_G)(+N_G)} \\ \vdots & \ddots & \vdots \\ \widetilde{H}_{(+N_G)(-N_G)} & \cdots & \widetilde{H}_{(+N_G)(+N_G)} \end{bmatrix} \begin{bmatrix} \tilde{a}_{(-N_G)} \\ \vdots \\ \tilde{a}_{(+N_G)} \end{bmatrix} = E \begin{bmatrix} \tilde{a}_{(-N_G)} \\ \vdots \\ \tilde{a}_{(+N_G)} \end{bmatrix} \tag{2-37}$$

where $$\widetilde{H}_{(m')(m)} = \int_0^d dz e^{i(G_m - G_{m'})} \cdot \left(\overline{\overline{H}}_{3\times 3}(k_z = G_m) + U(z)\cdot \overline{\overline{I}} \right) \tag{2-38}$$

and $$\tilde{a}_{(m')} = \begin{bmatrix} a_{m'n}^{1} \\ a_{m'n}^{2} \\ a_{m'n}^{3} \end{bmatrix}. \tag{2-39}$$

The $3(2N_G+1)$ eigenvalues E_n are the energy of each subband, while the $3(2N_G+1)$ eigenvectors yield the wavefunction by

$$\psi_n(z) \approx \frac{1}{\sqrt{A}} \sum_{j}^{c,lh,so} \sum_{m=-N_G}^{+N_G} a_{mn}^{j} e^{iG_m z} \cdot u_{j0}(\vec{r}_{\parallel}, z) \tag{2-40}$$

Here we neglect the $\vec{r}_{\parallel}$ dependence because $e^{i\vec{k}_{\parallel}\cdot\vec{r}_{\parallel}} \approx 1$ in the limit of $\vec{k}_{\parallel}\cdot\vec{r}_{\parallel} \ll 1$. After obtaining the envelop function, an average in-plane effective mass of each

conduction subband *n* is calculated as

$$\frac{1}{m_n^*} = \int_0^d dz \frac{\left|\psi_n(z)\right|^2}{m_j^*(z)} = \frac{1}{A}\int_0^d dz \sum_j \frac{\left|g_{n,j}(z)\right|^2}{m_j^*(z)} \tag{2-41}$$

where $m_j^*(z)$ is the effective mass of band *j* of the material at position z. The calculation makes use of the orthogonality of the cell functions

$$\int_{cell} u_{j0}^* u_{i0} d\vec{r} = \delta_{ij} . \tag{2-42}$$

Based on the average subband electron effective mass, the in-plane energy dispersion is approximated as parabolic

$$E_{n,\vec{k}} = E_n + \frac{\hbar^2 k_{\|}^2}{2m_n^*} . \tag{2-43}$$

2.2 X-valley electronic states

For (001)-grown QCL structures, due to the z direction confinement and the anisotropic X valley effective mass of the materials, the X valleys can be classified to two groups: X_z valley along the across-plane direction and X_x, X_y along the in-plane direction. The X_x and X_y valleys are equivalent from the effective mass point of view, and are regarded as one doubly degenerate X_x valley. The electron wavefunctions near the *X* valley bottom is expressed as

$$\psi_{n,\vec{k}}^{X_x}(\vec{r}_{\|}, z) = \frac{1}{\sqrt{A}} e^{i\left(\vec{k}\cdot\vec{r} + \frac{\pi}{a}x\right)} g_n^{X_x}(z) u^{X_x}(\vec{r}_{\|}, z) \tag{2-44}$$

$$\psi_{n,\vec{k}}^{X_z}(\vec{r}_{\|}, z) = \frac{1}{\sqrt{A}} e^{i\vec{k}\cdot\vec{r}} g_n^{X_z}(z) u^{X_z}(\vec{r}_{\|}, z) \tag{2-45}$$

Since the energies of *X* valleys are well above the valence bands and its coupling with the valence bands can be negligible. Therefore, *X* valley subband energies and wavefunctions can be directly obtained by solving the effective mass equation

$$\left[\frac{-\hbar^2}{2m_t^*(z)}\frac{d^2}{dz^2} + U_X(z)\right] g_n^{X_x}(z) = E_n^{X_x} g_n^{X_x}(z) \tag{2-46}$$

$$\left[\frac{-\hbar^2}{2m_l^*(z)}\frac{d^2}{dz^2}+U_X(z)\right]g_n^{X_z}(z)=E_n^{X_z}g_n^{X_z}(z) \tag{2-47}$$

$$U_X(z)=V_B^X(z)-|e|Fz-|e|\varphi(z) \tag{2-48}$$

where $V_B^X(z)$ is the band discontinuity of the X valley due to heterojunctions. Similarly, this differential equation can be solved by the reciprocal-space numerical approach, through which $g_n^{X_x}(z)$ and $g_n^{X_z}(z)$ are replaced by their Fourier expansions, and yields

$$\sum_{m',m}a_{mn}^{X_x}\frac{1}{d}\int_0^d dze^{i(G_m-G_{m'})z}\left[\frac{\hbar^2G_m^2}{2m_t^*(z)}+U_X(z)\right]=E_n^{X_x}a_{m'n}^{X_x} \tag{2-49}$$

$$\sum_{m',m}a_{mn}^{X_z}\frac{1}{d}\int_0^d dze^{i(G_m-G_{m'})z}\left[\frac{\hbar^2G_m^2}{2m_l^*(z)}+U_X(z)\right]=E_n^{X_z}a_{m'n}^{X_z} \tag{2-50}$$

Solutions to the eigenvalue problems provide $2N_G+1$ energy levels and the corresponding eigenvectors for the X_x or X_z subbands. Finally, the average subband effective mass and dispersion are calculated as

$$\frac{1}{m_{\xi n}^{\nu *}}=\frac{1}{A}\int_0^d dz\frac{\left|g_n^{\nu}(z)\right|^2}{m_{\xi}^*(z)},\quad \xi=l,t \quad\text{and}\quad \nu=X_x,X_z \tag{2-51}$$

$$E_{n,\vec{k}_{\|}}^{X_x}=E_n^{X_x}+\frac{\hbar^2k_{\|}^2}{2\sqrt{m_{ln}^{X_x*}m_{tn}^{X_x*}}} \tag{2-52}$$

$$E_{n,\vec{k}_{\|}}^{X_z}=E_n^{X_z}+\frac{\hbar^2k_{\|}^2}{2m_{tn}^{X_z*}} \tag{2-53}$$

3. Non-radiative and optical transitions

3.1 Polar longitudinal optical (LO) phonon scattering

In this section, electron polar LO-phonon scattering rates in a heterostructure system are derived. The optical phonons in such system are spatially confined similar to the electrons, and the interaction of confined electrons and phonons can be treated by several macroscopic models such as the dielectric continuum model [25, 26] and the hydrodynamic model [27]. However, the approximation of using dispersionless bulk phonons has been proved to provide decent estimate [28-30] and greatly simplify the scattering rate calculation. Therefore, unscreened bulk phonon modes of the well material are adopted in this work, since electrons most likely stays within the well material.

The scattering rate for an electron initially in state $\left|i,\vec{k}_i\right\rangle$ (subband i and in-plane wavevector $\vec{k}_i$) to the final state $\left|f,\vec{k}_f\right\rangle$ through an interaction potential H_{LO} is evaluated using Fermi's golden rule

$$S_{if}(\vec{k}_i,\vec{k}_f)=\frac{2\pi}{\hbar}\left|\left\langle f,\vec{k}_f\left|H'\right|i,\vec{k}_i\right\rangle\right|^2\delta\left(E_f(\vec{k}_f)-E_i(\vec{k}_i)\pm\hbar\omega_{LO}\right). \tag{3-1}$$

The subscript i here denotes a combination of indices $\left|i,\vec{k}_i\right\rangle=\left|(n_{\nu\lambda},\nu,\lambda),\vec{k}_i\right\rangle$ where ν is the valley index; λ is the stage index; and $n_{\nu\lambda}$ is the subband index. For polar LO phonon scattering, the same valley holds for both initial and final states. The electron-phonon interaction Hamiltonian has the form of

$$H_{LO}=\sum_{\vec{q}}\alpha(\vec{q})\left(e^{i\vec{q}\cdot\vec{r}}b_{\vec{q}}+e^{-i\vec{q}\cdot\vec{r}}b_{\vec{q}}^{\dagger}\right) \tag{3-2}$$

where $b_{\vec{q}}$ and $b_{\vec{q}}^{\dagger}$ are the creation and annihilation operator for a phonon in mode $\vec{q}$, and $\alpha(\vec{q})$ is the Frohlich electron-phonon interaction [31]

$$\left|\alpha(\vec{q})\right|^2=\frac{e^2\hbar\omega_{LO}}{2q^2}\left(\frac{1}{\varepsilon_\infty}-\frac{1}{\varepsilon_0}\right) \tag{3-3}$$

where ε_∞ and ε_0 are the static and high frequency permittivities.

The matrix element is calculated by [32]

$$\left|\left\langle f,\vec{k}_f\left|H_{LO}\right|i,\vec{k}_i\right\rangle\right|^2=\frac{e^2\hbar\omega_{LO}}{2V}\left(\frac{1}{\varepsilon_\infty}-\frac{1}{\varepsilon_0}\right)\left(n_{\omega_{LO}}+\frac{1}{2}\mp\frac{1}{2}\right)$$

$$\times\frac{1}{q_z^2+q_{||}^2}\left|A_{if}(q_z)\right|^2\delta_{\vec{k}_i,\vec{k}_f\mp\vec{q}_{||}} \tag{3-4}$$

where $\vec{q}_{||}$ and $\vec{q}_z$ are the in-plane and cross-plane components of the phonon wavevector; $n_{\omega_{LO}}$ is the Bose-Einstein occupation, and the upper and lower signs correspond to phonon absorption and emission, respectively; $\delta_{\vec{k}_i,\vec{k}_f\mp\vec{q}_{||}}$ ensures in-plane momentum conservation; $A_{if}(q_z)$ is the form factor calculated by

$$A_{if}(q_z)=\int_0^d dz\psi_f^*(z)\psi_i(z)e^{\pm q_z z}. \tag{3-5}$$

The envelope wavefunction $\psi_i(z)$ for each subband are obtained using **k·p** method for Γ valley subbands and effective mass approach for *X* valley subbands. The available final states also need to satisfy the energy conservation condition

$$E_f(0)+\frac{\hbar^2k_f^2}{2m_f^*}=E_i(0)+\frac{\hbar^2k_i^2}{2m_i^*}\mp\hbar\omega_{LO}. \tag{3-6}$$

Combine the energy conservation condition and the momentum conservation rule, the restriction of the final state can be derived

$$q_{||}=\frac{\sqrt{2}}{\hbar}\left[m_i^*E_i(\vec{k}_i)+m_f^*E_f(\vec{k}_f)-2\sqrt{m_i^*m_f^*E_i(\vec{k}_i)E_f(\vec{k}_f)}\cos\theta\right]^{\frac{1}{2}} \tag{3-7}$$

where θ is the angle between the in-plane wavevectors $\vec{k}_i$ and $\vec{k}_f$. Integrating the transition rate $S_{if}(\vec{k}_i,\vec{k}_f)$ over all possible $\vec{k}_f$ provides the total scattering rate for an electron transiting from an intial state $\left|i,\vec{k}_i\right\rangle$ to subband *f*

$$W_{if}(\vec{k}_i)=\frac{m_f^*e^2\hbar\omega_{LO}}{8\pi\hbar^2}\left(\frac{1}{\varepsilon_\infty}-\frac{1}{\varepsilon_0}\right)\left(n_{\omega_{LO}}+\frac{1}{2}\mp\frac{1}{2}\right)\int_0^{2\pi}d\theta B_{if}(q_{||})$$

$$\times\vartheta\left(E_i(\vec{k}_i)+E_i-E_f\pm\hbar\omega_{LO}\right) \tag{3-8}$$

where $B_{if}(q_{||})$ is given by

$$B_{if}(q_{||})=\int_0^d dz\int_0^d dz'\psi_f^*(z)\psi_i(z)\psi_i^*(z')\psi_f(z')\frac{1}{q_{||}}e^{-q_{||}|z-z'|}. \tag{3-9}$$

For Γ valley, this integral can be evaluated by

$$B_{if}^{\Gamma}(q_{\|}) = \int_0^d dz \int_0^d dz' \sum_{j,j'} g_{f,j}^*(z) g_{i,j}(z) g_{i,j'}^*(z') g_{f,j'}(z') \frac{1}{q_{\|}} e^{-q_{\|}|z-z'|}, \qquad (3\text{-}10)$$

while it can directly calculated for X valley. The intrasubband scattering rate can also be calculated by setting $i = f$ and then $\psi_i(z) = \psi_f(z)$.

3.2 Intervalley scattering

The phonon assisted intervalley $\Gamma - X_x$ and $\Gamma - X_z$ electron transitions can be modeled through an intervalley deformation potential [33]. Again, the electrons are assumed to interact with bulk intervalley phonons. The scattering rate from the initial ν valley state $\left|i, \vec{k}_i\right\rangle = \left|(n_{\nu\lambda}, \nu, \lambda), \vec{k}_i\right\rangle$ to the final ν' valley ($\nu' \neq \nu$) subband $f = (n_{\nu'\lambda'}, \nu', \lambda')$ is given by

$$W_{if}(\vec{k}_i) = \frac{Z_{\nu'} D_{\nu\nu'}^2 m_f^*}{2\hbar\rho(\hbar\omega_{\nu\nu'})} \left(n_{\nu\nu'} + \frac{1}{2} \mp \frac{1}{2} \right) I_{if} \vartheta\left(E_i(\vec{k}_i) + E_i - E_f \pm \hbar\omega_{\nu\nu'} \right) \qquad (3\text{-}11)$$

where $D_{\nu\nu'}$ is the intervalley ($\nu - \nu'$) deformation potential constant, ρ is the mass density, and $\hbar\omega_{\nu\nu'}$ is the intervalley phonon energy; $n_{\nu\nu'}$ is the equilibrium intervalley phonon occupancy, and $Z_{\nu'}$ is the degeneracy of the final valley ($Z_{\Gamma} = 1, Z_{X_z} = 1$, and $Z_{X_x} = 1$ for intervally $X_x - X_x$, 2 for the others). The overlap integral is

$$I_{if} = \int_0^d dz \left|\psi_i(z)\right|^2 \left|\psi_j(z)\right|^2. \qquad (3\text{-}12)$$

3.3 Electron-electron (e-e) scattering

The effect of electron-electron scatterings is to change the energy of each individual electron, while keep the energy of the global electron system unchanged [34]. In QCLs, e-e scattering is expected to be important to promote intersubband transitions between closely separated subbands at low temperature when LO-phonon scattering is weak [35]. The e-e interaction can be divided into the binary e-e

scattering and electron-plasmon coupling, and the latter is neglected because it is only important for highly doped devices [36]. Since typically the *X* valley population is high only at very high fields above threshold, the e-e scattering is only taken into account for Γ subbands.

We consider a "target" electron in state $\left|i,\vec{k}_i\right\rangle$ interacts with a "partner" electron in state $\left|j,\vec{k}_j\right\rangle$, and after interaction they are scattered into states $\left|f,\vec{k}_f\right\rangle$ and $\left|g,\vec{k}_g\right\rangle$, respectively. The interaction Hamiltonian can be written as

$$H_{e-e}=\frac{e^2}{4\pi\varepsilon R} \tag{3-13}$$

where R is the distance between two electron

$$R=\sqrt{(\vec{r}-\vec{r}')^2+(z-z')^2}\ . \tag{3-14}$$

$\vec{r}$ and z are the coordinate for the target electron, while $\vec{r}'$ and z' are for the partner electron. The wavefunction of the initial joint state of the two electrons is given by

$$\left|i,\vec{k}_i;j,\vec{k}_j\right\rangle=\frac{1}{\sqrt{A}}e^{-i\vec{k}_i\cdot\vec{r}}\psi_i(z)\frac{1}{\sqrt{A}}e^{-i\vec{k}_j\cdot\vec{r}'}\psi_j(z') \tag{3-15}$$

The matrix element can be evaluated by

$$\left\langle f,\vec{k}_f;g,\vec{k}_g\left|H_{e-e}\right|i,\vec{k}_i;j,\vec{k}_j\right\rangle=\frac{e^2}{4\pi\varepsilon_\infty}\int_{-\infty}^{+\infty}\int_{-\infty}^{+\infty}dzdz'\psi_f^*(z)\psi_g^*(z')\psi_i(z)\psi_j(z')$$

$$\times\frac{1}{A^2}\int_{-\infty}^{+\infty}\int_{-\infty}^{+\infty}d^2\vec{r}d^2\vec{r}'\frac{e^{-i(\vec{k}_i-\vec{k}_f)\cdot\vec{r}}e^{-i(\vec{k}_j-\vec{k}_g)\cdot\vec{r}}}{\sqrt{(\vec{r}-\vec{r}')^2+(z-z')^2}} \tag{3-16}$$

After obtaining the matrix element, the calculation of the transition rate is straight forward by applying the Fermi's golden rule. Summation of the transition rate over all possible final states for the partner electron provides the total e-e scattering rate

$$W_{if}(\vec{k}_i)=\frac{e^4m_f^*}{32\pi\hbar^3\varepsilon_\infty^2A}\sum_{\vec{k}_j,\sigma}\sum_{j,g}f_j(\vec{k}_j)\left[1-f_f(\vec{k}_f)\right]\left[1-f_g(\vec{k}_g)\right]$$

$$\times\int_0^{2\pi}d\theta\frac{\left|F_{ijfg}(q)\right|^2}{q^2\varepsilon^2(q)}+\frac{\left|F_{ijfg}(q')\right|^2}{q'^2\varepsilon^2(q')}-\frac{\left|F_{ijfg}(q)\right|\left|F_{ijfg}(q')\right|}{q\varepsilon(q)q'\varepsilon(q')} \tag{3-17}$$

where σ accounts the spins; $f_j(\vec{k}_j)$ is the distribution function, and $F_{ijfg}(q)$ is the e-e form factor given by

$$F_{ijfg}(q)=\int_0^d\int_0^d dzdz'\psi_f^*(z)\psi_g^*(z')\psi_i(z)\psi_j(z')e^{-q|z-z'|} \tag{3-18}$$

$$q=\frac{1}{2}\left[2k_{fi}^2+k_0^2-2k_{fi}\sqrt{k_{fi}^2+k_0^2}\cos\theta\right]^{1/2} \tag{3-19}$$

$$q'=\frac{1}{2}\left[2k_{fi}^2+k_0^2+2k_{fi}\sqrt{k_{fi}^2+k_0^2}\cos\theta\right]^{1/2} \tag{3-20}$$

The wavevectors are given by

$$\vec{k}_{fi}=\vec{k}_f-\vec{k}_i,\ \ k_0=\frac{2}{\hbar}\left[m_i^*(E_i+E_j-E_f-E_g)\right]^{1/2} \tag{3-21}$$

The e-e scattering rate in the presence of distribution function is calculated by the rejection technique [37]. Since each electron in the transport simulation can act as both "target" and "partner" electron, the actual scattering rate should be divided by 2. In addition, it is necessary to update the momentums and energies of both electrons in order to maintain the conservation [38].

3.4 Optical transitions

The interaction Hamiltonian between an electron and a photon is given by [15]

$$H_{op}\approx\frac{e}{m^*}\vec{A}\cdot\vec{p}. \tag{3-22}$$

The Lorentz-gauge vector potential A for a harmonic interaction can be written in term of the raising and lowering operators $a^\dagger_{\vec{k}_{op},\sigma}$ and $a_{\vec{k}_{op},\sigma}$:

$$\vec{A}=\sqrt{\frac{\hbar}{2\varepsilon\omega_{\vec{k}_{op}}V}}\hat{e}_{\vec{k}_{op},\sigma}\left[a_{\vec{k}_{op},\sigma}e^{i\vec{k}_{op}\cdot\vec{r}}+a^\dagger_{\vec{k}_{op},\sigma}e^{-i\vec{k}_{op}\cdot\vec{r}}\right] \tag{3-23}$$

where ε is the permittivity, V is the volume of the cavity, $\omega_{\vec{k}_{op}}$ is the photon frequency, and $\hat{e}_{\vec{k}_{op},\sigma}$ is the polarization vector. Apply the similar procedure as the calculation of non-radiative scattering rate, the obtained photon emission rate can be separated by spontaneous emission and stimulated emission as follows [35]:

$$W_{if}^{(sp)} == \frac{\pi e^2 \omega_{\bar{k}_{op}}}{\varepsilon V} \left| \hat{e}_{\bar{k}_{op},\sigma} \cdot \hat{z} \right|^2 \left| z_{if} \right|^2 \delta(E_f - E_i + \hbar\omega_{\bar{k}_{op}}) \tag{3-24}$$

$$W_{if}^{(st)} = \frac{\pi e^2 \omega_{\bar{k}_{op}}}{\varepsilon V} \left| \hat{e}_{\bar{k}_{op},\sigma} \cdot \hat{z} \right|^2 \left| z_{if} \right|^2 \delta(E_f - E_i + \hbar\omega_{\bar{k}_{op}}) n_{\bar{k}_{op},\sigma} \tag{3-25}$$

where the superscript "*sp*" and "*st*" denote "spontaneous" and "stimulated", respectively; $n_{\bar{k}_{op},\sigma}$ is the number of photons in the mode; and z_{if} is the dipole matrix element calculate by

$$z_{if} = \langle f | z | i \rangle = \int_0^d z \psi_f^*(z) \psi_i(z) dz \tag{3-26}$$

The dipole matrix element is one of the most important parameters that characterize the performance of a QCL, which represents the optical coupling strength between the two subbands.

4. Ensemble Monte Carlo simulation

4.1 Transport equation for QCLs

Electron transport in modern semiconductor devices can be depicted by the Boltzmann transport equation (BTE). The BTE is a continuity equation that describes particle flow in a six-dimensional position-momentum space [39]

$$\frac{\partial f}{\partial t}+\vec{v}\cdot\nabla_{\vec{r}}f+\frac{d\vec{p}}{dt}\cdot\nabla_{\vec{p}}f = \sum_{\vec{k}'}\left\{S(\vec{k}',\vec{k})f(\vec{k}')[1-f(\vec{k})]-S(\vec{k},\vec{k}')f(\vec{k})[1-f(\vec{k}')]\right\} \quad (4\text{-}1)$$

where the function $f(\vec{r},\vec{p},t)$ ($\vec{p}=\hbar\vec{k}$) is the electron distribution function, which gives the probability of find electrons at time t, located at position $\vec{r}$, with momentum $\vec{p}$. The second and third tem in the left-hand side (LHS) describe the net flow of electrons into an elementary volume centered at $\vec{r}$ in position space and $\vec{p}$ in momentum space. The right-hand side (RHS) is the collision integral denotes the net in-scattering rate, in which $S(\vec{k},\vec{k}')$ represents the transition rate from an initial state $\left|\vec{k}\right\rangle$ to a final state $\left|\vec{k}'\right\rangle$. The BTE treats the scatterings as instantaneous events that only change the momentum of an electron.

The BTE is a semi-classical approach to describe carrier transport, since the definition of distribution function conflicts with the uncertainty principle who states that position and momentum cannot be simultaneously known to arbitrarily high precision. It is well suitable when the spatial variation of external potential is much greater than the de Broglie wavelength and the transport time is much larger than the time interval between scatterings.

In QCLs, since electrons have wavelike behavior in confined cross-plane direction (*z* direction), the electric field applied along this direction does not explicitly accelerate electrons, but affects the electron distribution by modifying the band profiles. Therefore, based on the BTE framework, the electron transport in z direction is purely scattering between subbands, which is also called “hopping transport”. On the other hand, there is no field or doping variation along the in-plane direction, and

hence the second and third terms in the LHS of the BTE can be eliminated. Based on the discussion above, the Boltzmann like transport equation for QCLs can be written as [40]

$$\frac{d}{dt} f_{i,\vec{k}_i} = \sum_{f,\vec{k}_f} \left\{ S_{fi}(\vec{k}_f, \vec{k}_i) f_f(\vec{k}_f)[1 - f_i(\vec{k}_i)] - S_{if}(\vec{k}_i, \vec{k}_f) f_i(\vec{k}_i)[1 - f_f(\vec{k}_f)] \right\}. \qquad (4\text{-}2)$$

4.2 Ensemble Monte Carlo method

The ensemble Monte Carlo (EMC) method, as applied to charge transport in semiconductors, is a method directly solve the BTE. It consists of a simulation of the motion of many electrons inside the crystal, subject to the presence of external forces due to applied electric and magnetic fields and of given scattering mechanisms [41, 42]. As illustrated in Fig. 4.1, the simulation starts with preparing a group of electrons in an initial condition with given wave vectors (or momentums). Then the electrons begin to move, and their motions can be described by the combination of two different processes – free flights driven by the external force and scatterings due to the collisions with other particles, such as phonons, impurities or even other electrons. The transport keeps evolving with alternative occurrences of free flights and scatterings until the total simulation time is reached or the specified precision is satisfied. During the simulation, we observe and obtain the average transport quantities such as energy, momentum or position after each time step dt. Because the duration of a collision is typically much shorter than the duration of the free flight between collisions, collisions are treated as instantaneous events. Thus the essential tasks for the EMC are to determine when the collisions occur (in other words, the free flight duration); and how electrons scatter.

In the EMC, the free flight duration is determined by a random number whose average value can be pre-calculated by the scattering rates. After a free flight, the EMC method assumes that only one scattering mechanism will take place, and its selection is also realized by a random number. The probability that a particular

scattering mechanism is chosen can be inferred as the portion of its rate in the total scattering rate. Finally, the electron's kinetic energy after scattering is determined through the energy conservation law. On the other hand, the direction of its momentum is determined by another random number whose distribution maintains the momentum conservation law.

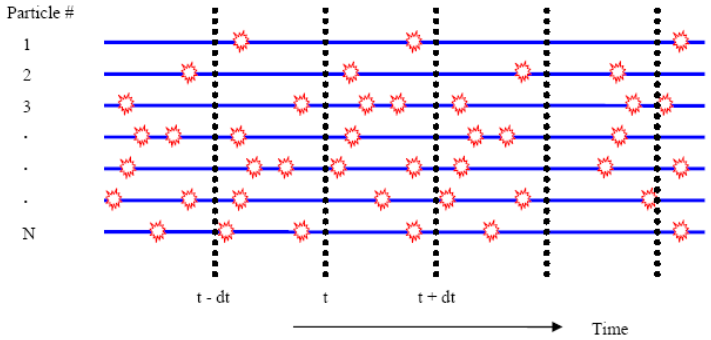

Fig. 4.1 Flight dynamics of the ensemble Monte Carlo method

Follow the characteristics of QCLs, the free flight of electrons are only allowed along the in-plane direction, while in the cross-plane direction, the intersubband scatterings model the transport. The flowchart of a typical EMC simulation described above is shown in Fig. 4.2. Since the wavefunctions between subbands localized in two spatially remote stages have very little overlap, the probability of scatterings between them is fairly small. For this reason, the subbands in one stage are considered only coupling with the subbands in the two neighboring stages. Such nearest-neighbor approach plus the translation feature of the wavefunctions in QCL structures enable us to reduce the modeled region to a single stage. In order to maintain the charge conservation in the simulated stage under steady state, any electron scattered out of one side of the stage will be scattered back from the translational symmetric subband on the other side. The current can be evaluated at the interface between two stages, through counting the net scattering events per unit time between the two subbands whose wavefunctions are localized in the two stages, respectively.

The photons are not explicitly modeled in the EMC, but their emission can be reflected by the optical dipole matrix element between two subbands.

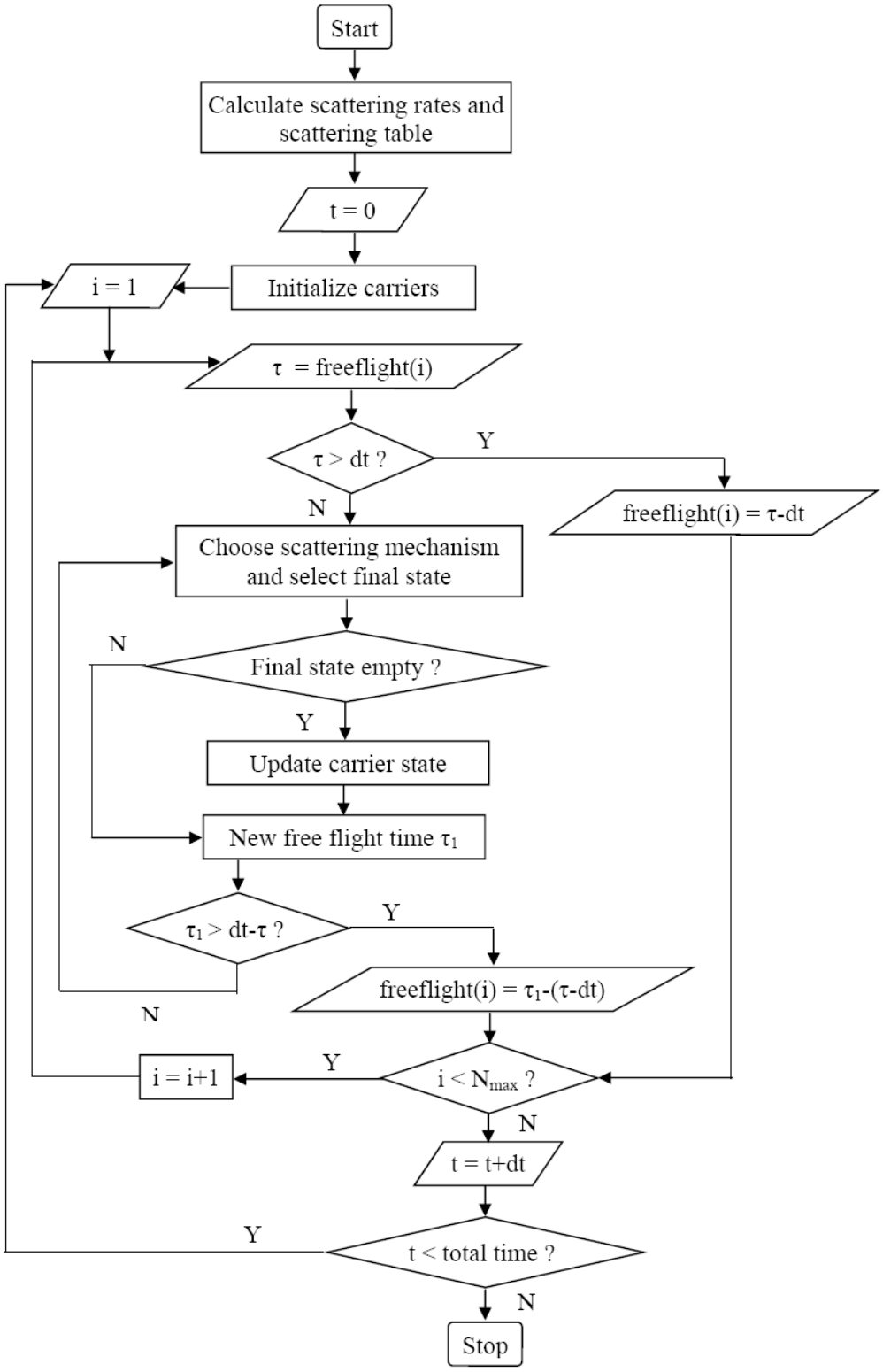

Fig. 4.2 Flowchart of the ensemble Monte Carlo transport simulation for QCLs [36].

5. Simulation results

5.1 9.4 μm 45% GaAs/AlGaAs QCL

The first device investigated is a double-quantum-well GaAs based mid-infrared QCL [13]. Its emitting wavelength is about 9.4μm with threshold field 48 kV/cm, and the composition of the barrier material is $Al_{0.45}Ga_{0.55}As$. The thickness of the layers in one stage in the unit of angstrom, starting from the injection barrier, are **46**, 19, **11**, 54, **11**, 48, **28**, 34, **17**, 30, **18**, 28, **20**, 30, **26**, 30. The bold script denotes the barriers, the normal script are the wells, and the underlined script denotes the n-type doped regions with a sheet density of $N_s = 3.8\times10^{11}$ cm^{-2}.

Fig 5.1 shows the energy levels and wavefunction moduli squared of the Γ- (a) and X-valley (b) subbands in two adjacent stages, at the above threshold field F = 53 kV/cm and the lattice temperature T = 77 K. The three black bold states per stage in Fig. 5.1(a), from the lowest to the highest, are the ground level, lower lasing level and upper lasing level, respectively, and are denoted as 1, 2, and 3. The radiative transition takes place from state 3 to 2. The green and red states are two Γ-continuum states above the upper lasing level. The calculated dipole matrix element between the upper and lower lasing levels is z_{32}=1.6 nm.

Selected form factors for electron-LO and electron-electron scattering rates calculation are shown in Fig. 5.2 and 5.3, respectively. Both the two figures indicate that the intrasubband scatterings should take place more frequently than the intersubband scatterings. The electric field vs current density characteristics at the lattice temperature of 77 K and 300 K are shown in Fig. 3.4. The calculated threshold current of J_{th} = 2.9 kA/cm^2 at 77 K is obtained in the simulation, and agrees well with the experimental result of 3 kA/cm^2 [13].

Fig. 5.4 presents how the valley population changes with the electric field and the lattice temperature. According to the figure, the X-valley population increase with both field and temperature. High field and temperature enhance the in-plane kinetic energy of electrons, and facilitate their transitions from the lower-energy Γ valley to the higher-energy X valley over the energy difference. Since the X valley electrons do not contribute to lasing, they can be considered as leaked electrons. At 300 K and very high field, the X valley population may approach or even be higher than the Γ valley population. Therefore, it indicates that the considerable X valley leakage is the mechanism that may kill the lasing condition under the high-temperature operation [43, 44].

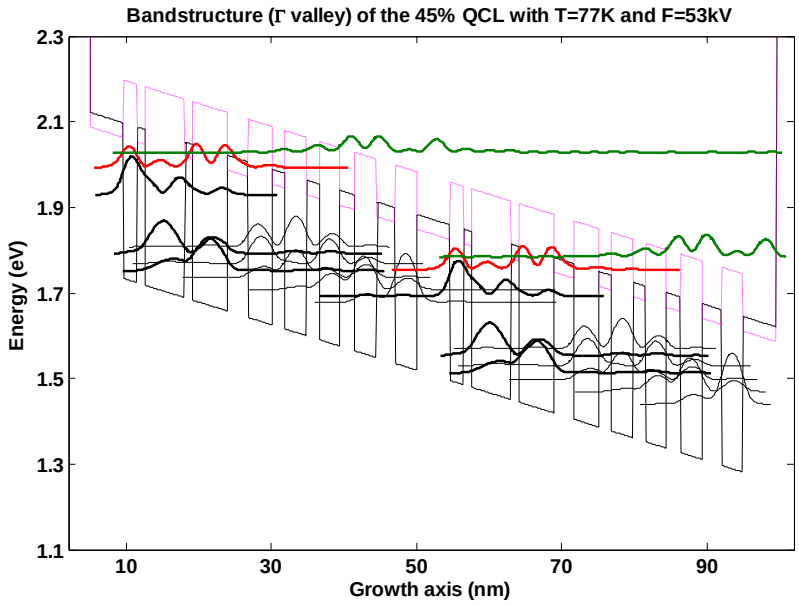

(a)

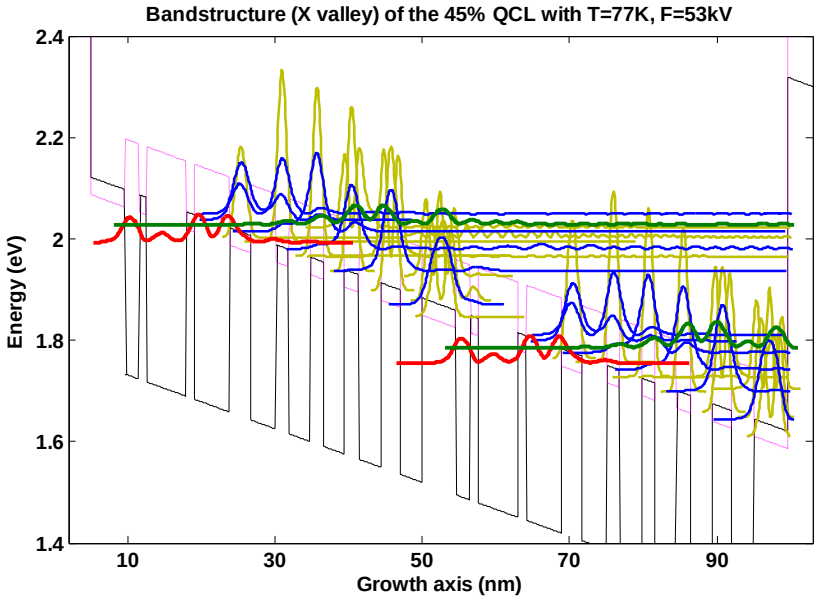

(b)

Fig. 5.1 The energy levels and wavefunction moduli squared of the Γ- (a) and X-valley (b) subbands for the 9.4 μm 45% GaAs/AlGaAs QCL at the electric field of 53 kV/cm and the lattice temperature of 77 K, where the green and red lines are two Γ-minibands above the upper lasing level.

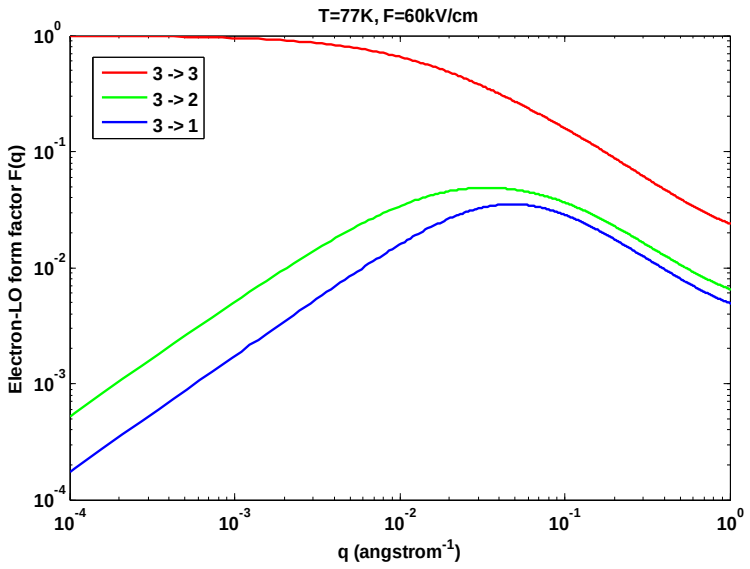

Fig. 5.2 Selected form factors for intrasubband (3→3) and intersubband (3→2, 3→1) electron-LO scattering for the 9.4 μm 45% GaAs/AlGaAs QCL, where 2 and 3 are the lower and upper lasing level, respectively; and 1 is the ground level.

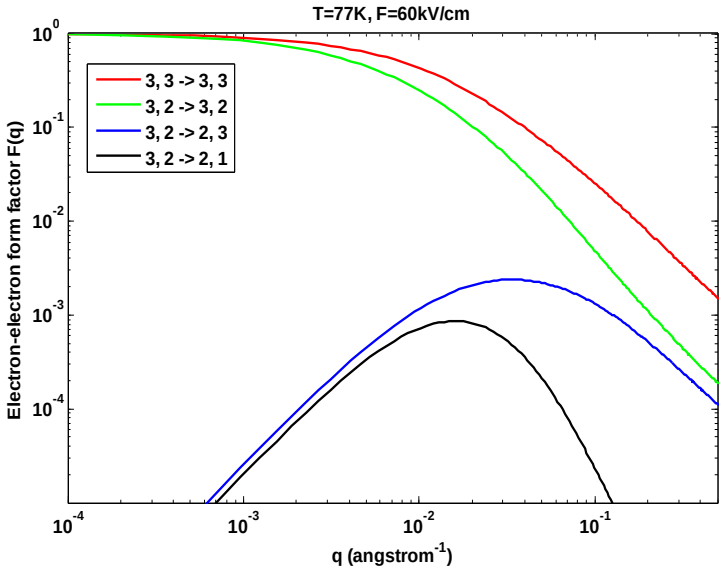

Fig. 5.3 Selected form factors for electron-electron scattering for the 9.4 μm 45% GaAs/AlGaAs QCL, where 2 and 3 are the lower and upper lasing level, respectively; and 1 is the ground level. In the legend, (i, j) → (f, g) denote the "target" electron is scattered from subband i to f, while the "partner" electron is scattered from subband j to g.

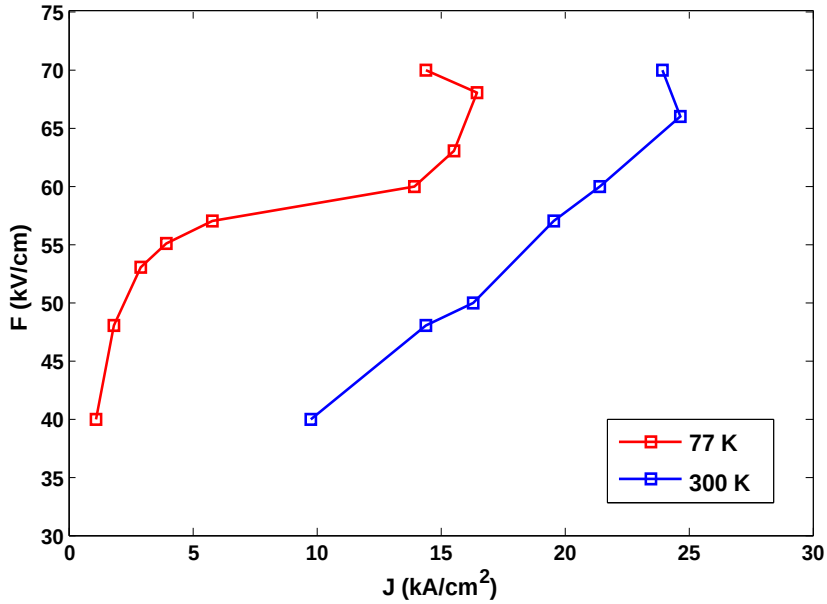

Fig. 5.4 Electric field vs current density characteristics for the 9.4 μm 45% GaAs/AlGaAs QCL at the lattice temperature of 77 K and 300 K.

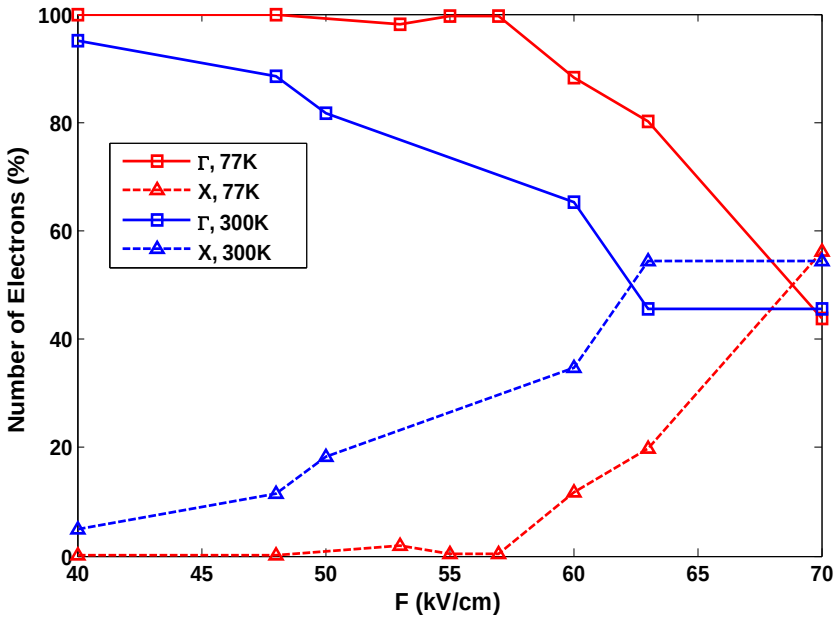

Fig. 5.5 Electric population in Γ and X valleys vs electric field for the 9.4 μm 45% GaAs/AlGaAs QCL at the lattice temperature of 77 K and 300 K.

5.2 4.8 μm deep-well InGaAs/AlInAs QCL

The second device modeled by the EMC is a deep-well InP based QCL [14]. For strain compensation in the InGaAs/AlInAs heterostructure, the Al content in the barriers in and around the active region is increased from 56% to 75%, thus providing much taller barriers. The tall barrier provides better confinement, which results in the suppress of the leakage path from the upper lasing level to the upper minibands by increasing their energy separation. Another modification is that the relaxation region has a tapered conduction-band edge, which pushes the wavefunctions of upper minibands or continuum states spatially away from the upper lasing level. In addition, the double-resonant design provides two subbands to depopulate the lower lasing level through the LO-phonon emission, and improves the population inversion.

The layer thicknesses, in angstroms, for one period of the QCL structure starting with the injection barrier, are: ***22***, [27], [*19*], [24], [*19*], [23], *20*, 21, *20*, 20, *22*, 18, *23*, 17, *23*, 17, *24*, ***12***, 14, ***11***, **46**, ***11***, **42**, ***12***, **38**. The bold normal script are $In_{0.68}Ga_{0.32}As$ wells, bold italic script are $Al_{0.75}In_{0.25}As$ barriers, normal script are $In_{0.60}Ga_{0.40}As$ wells, italic script are $Al_{0.56}In_{0.44}As$ barriers, underlining indicates doping at 1.4×10^{17} cm^{-3} in the QWs and 10^{17} cm^{-3} in the barriers. The bracketed layers are in the graded part of the relaxation/injection region: one $In_{0.66}Ga_{0.34}As$ well, two $In0._{64}Ga_{0.36}As$ wells, and two $Al_{0.65}In_{0.35}As$ barriers. The structure is effectively strain compensated with a nominal net strain of 0.01%, and has 30 periods. At an applied field of 75 kV/cm, the design parameters for this four-level laser system are 1.35 nm for the dipole matrix element.

Fig 5.6 shows the energy levels and wavefunction moduli squared of the Γ- (a) and X-valley (b) subbands in two adjacent stages, at the designed threshold field F = 75 kV/cm and the lattice temperature T = 77 K. Apparently, there is one additional injection state below the lower lasing level in comparison with Fig. 5.1(a), which forms the four-level laser system. Similarly, from the lowest to the highest, we can label the key states – 1 and 2 for the two injection states; 3 and 4 for lower and upper lasing level, respectively. The radiative transition takes place from state 4 to 3. The calculated dipole matrix element between them is z_{43}=1.35 nm. The green and red states are two Γ-continuum above the upper lasing level. Unlike the 9.4 μm QCL whose Γ-continuum states located in the energy range of X valley subbands, the X valley subbands in the 4.8 μm QCL are well above the upper lasing level as well as the Γ-continuum states. Consequently, the X valley leakage is expected to be

negligible, which is supported by Fig. 5.7 and 5.8. Fig. 5.7 shows that even at room temperature with very high bias, the X valley population is small due to the huge energy barrier between Γ-subbands and X-subbands. Fig. 5.8 demonstrates that the X valley can be safely neglected in the EMC simulation.

Electron distributions as a function of the in-plane kinetic energy at 77 K and 300K are shown in Fig. 5.9(a) and (b), respectively. It is clear that the distribution in each subband is driven to a displaced Maxwellian profile. As the temperature increases, the distribution is pushed toward the high-energy region, but the Maxwellian shape is kept. The inclusion of e-e scattering in the simulation is responsible for this phenomenon [45]. The e-e scattering strongly increases intersubband electron redistribution, and enhance the population of the upper lasing level. Finally, the time evolutions of the electron density in the subbands are plotted in Fig. 5.10(a) for 77 K and (b) for 300 K. The population inversion can be clearly seen from the figures. In addition, the population of two upper minibands increases with temperature, which implies escape from the Γ-continuum can be the main leakage mechanism for this QCL operating at room temperature.

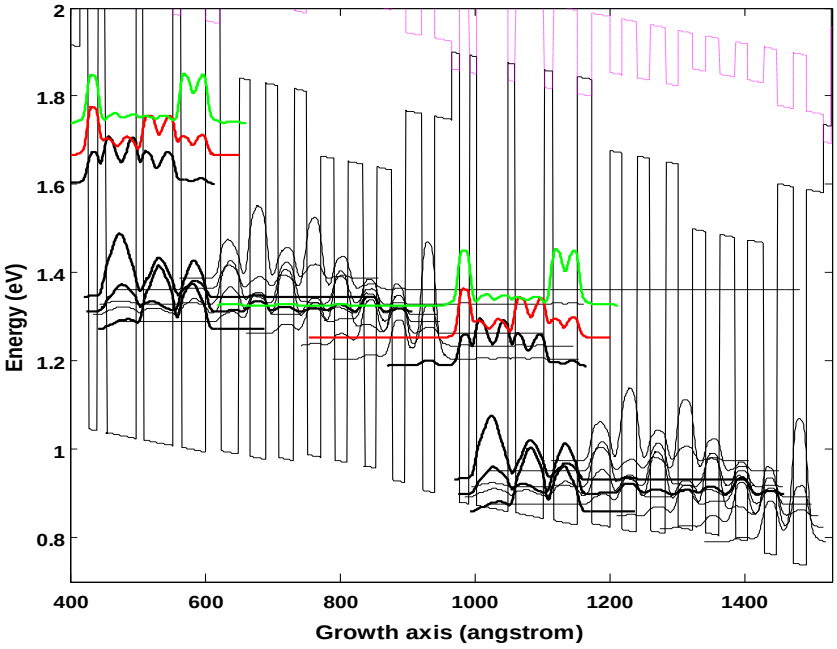

(a)

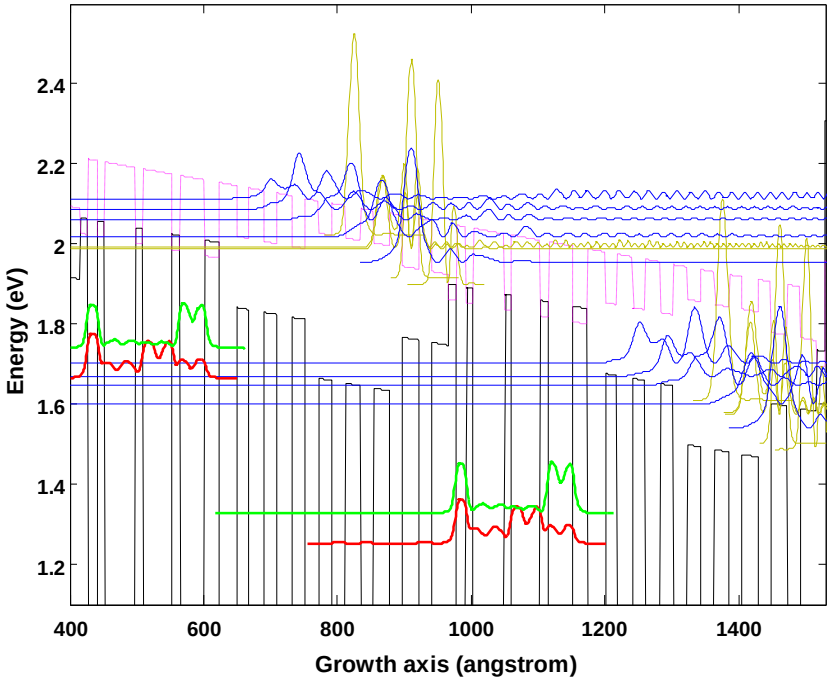

(b)

Fig. 5.6 The energy levels and wavefunction moduli squared of the Γ- (a) and X-valley (b) subbands for the 4.8 μm DW QCL at the electric field of 75 kV/cm and the lattice temperature of 77 K, where the green and red lines are two Γ-minibands above the upper lasing level.

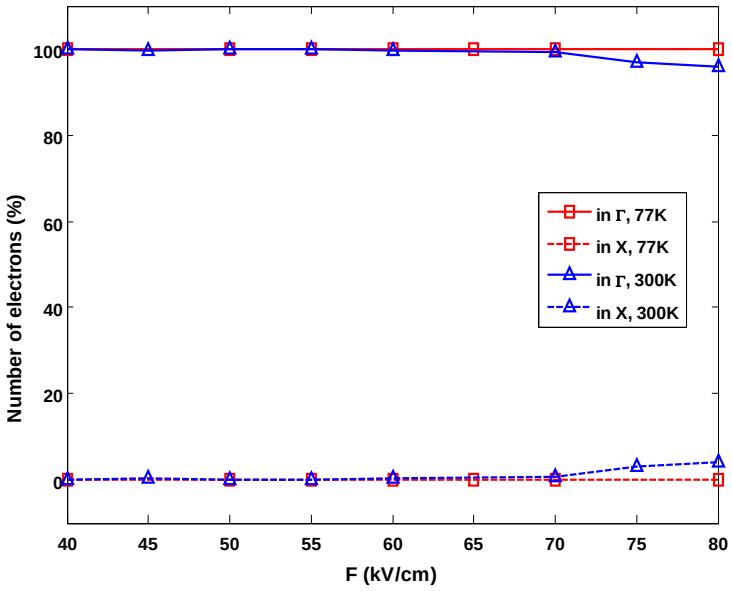

Fig. 5.7 Electric population in Γ and X valleys vs electric field for the 4.8 μm DW QCL at the lattice temperature of 77 K and 300 K.

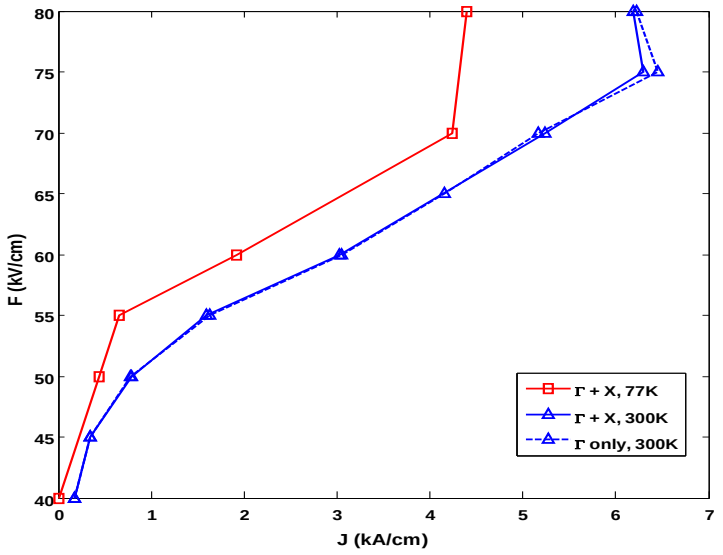

Fig. 5.8 Electric field vs current density characteristics for the 4.8 μm DW QCL at the lattice temperature of 77 K and 300 K.

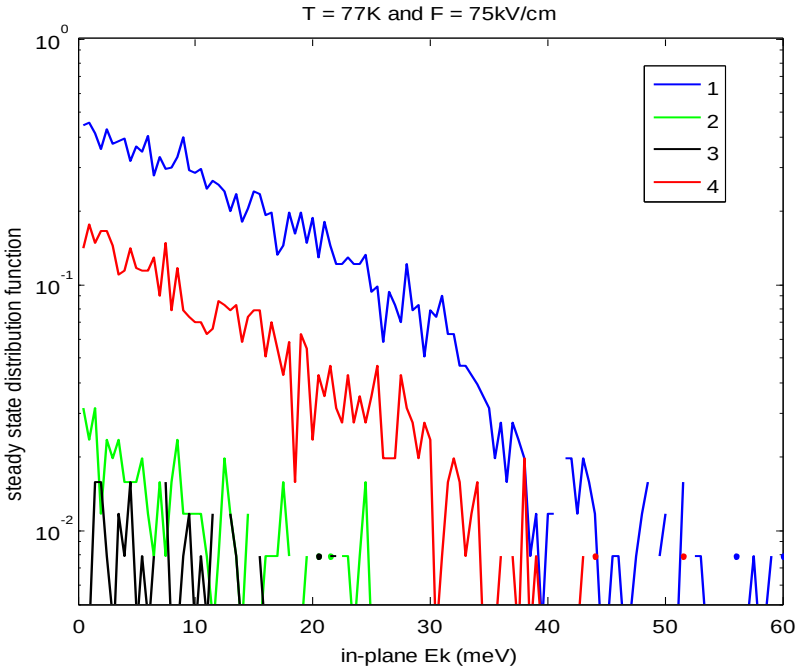

(a)

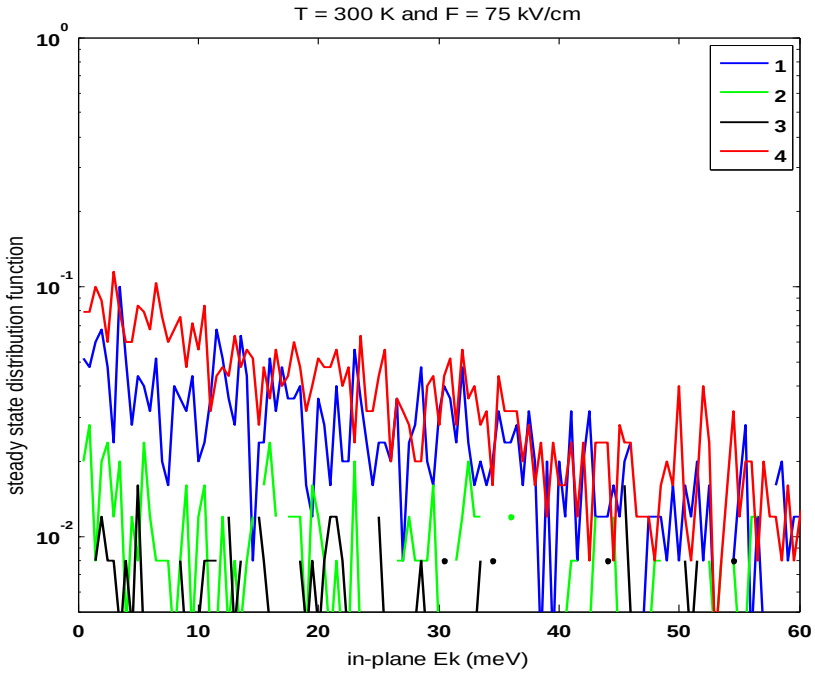

(b)

Fig. 5.9 Electron distributions of selected subbands as a function of the in-plane kinetic energy at F = 75 kV/cm and (a) T = 77 K and (b) T = 300 K, for the 4.8 μm DW QCL. In the legend, 1 and 2 are the injector states; 3 and 4 are the lower and upper lasing level, respectively.

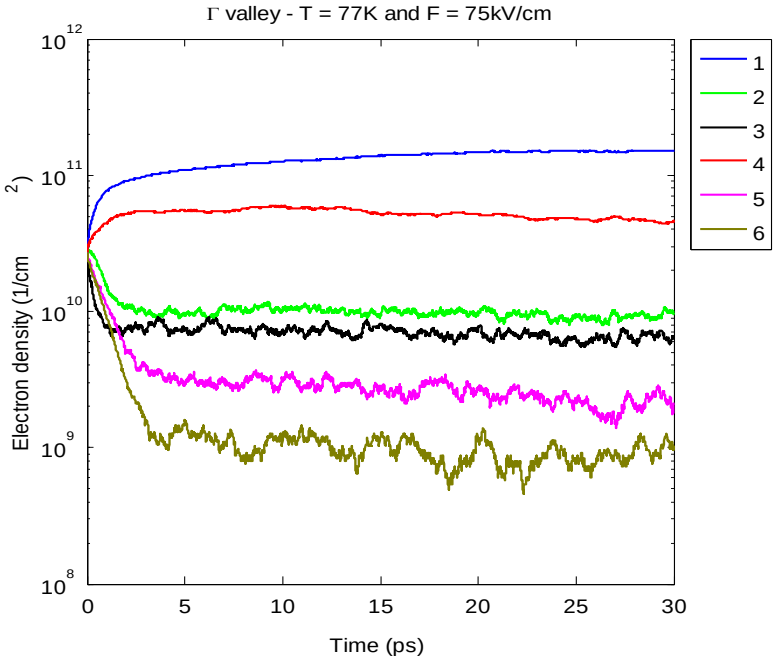

(a)

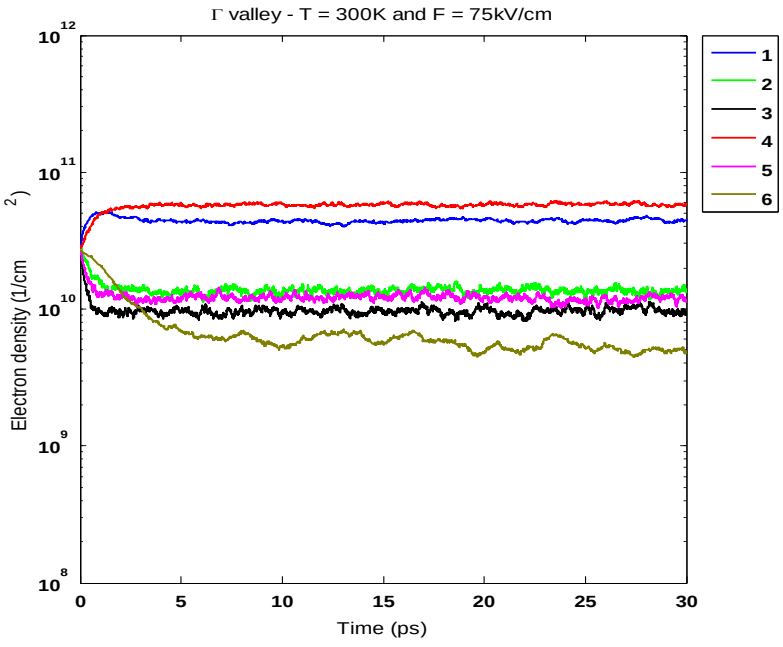

(b)

Fig. 5.10 Time evolution of the electron density in the selected subbands at F = 75 kV/cm and (a) T = 77 K and (b) T = 300 K, for the 4.8 μm DW QCL. In the legend, 1 and 2 are the injector states; 3 and 4 are the lower and upper lasing level, respectively; 5 and 6 are two minibands above the upper lasing level.

Conclusion and future work

In this project, we first derive the method for calculating the electron states in QCLs. The eight band **k·p** model is extended to the heterostructure case to calculate the Γ-valley subbands, in which the differential equations are solved by a reciprocal-space numerical technique. Owning to the weak coupling between conduction and valance band in the X valley, the effective mass equation is adopted to calculate the X valley subbands. Then the transition rates due to various non-radiative or radiative scattering mechanisms are derived based on the Fermi's golden rule. Thus, an Ensemble Monte Carlo method suitable for modeling the "hopping transport" in QCLs is introduced. Finally, two QCLs are simulated. The simulation not only provides quantitive prediction of the device output characteristics, but also enable us to analyze the leakage mechanism.

The current simulation framework assumes QCLs are operating under the isothermal condition, while in reality they may have localized hot spots due to the highly non-equilibrium transport. The performance of QCLs rapidly degrades due to the enormous internal (electron and lattice) heating. Temperature measurement of such nanometer scale devices is very difficult, and hence developing a simulation tool that can also offer the insight on the heat generation and the temperature distribution is emergent. Thermal and electronic transports in a QCL device are inherently coupled. The hot electrons energized by the applied electrical field eventually lose the energy to the crystal lattice through multiple-phonon emission processes, which lead to nonequilibrium optical phonons. These optical phonons do not conduct heat because of their near-zero group velocity, but they decay to acoustic phonons, which have large group velocity and can thus efficiently transfer the heat, contributing to the heat conductivity. In this process, the electron and phonon dynamics interact with each other in complicated ways. So a systematic model, which can simultaneously explain the electronic and thermal properties of a QCL device, should be a self-consistent solution of both the electron and phonon (thermal) transport equations. With the Monte Carlo electron transport simulator already developed, we would need to develop the phonon transport simulator and couple it to the electron transport part. Nevertheless, this kind of fully-coupled microscopic electron and phonon simulation will face serious challenges in terms of computation efficiency. There is another immediate difficulty that has to be pointed out: the incompatibility of computation domains. The electron transport is simulated in a very small fraction of a QCL device,

usually two or two and half stages, while the thermal transport needs to be considered in a whole device including the waveguide, so a smart way to connect the electron and thermal transport simulations is ultimately necessary.

Reference

[1] R. F. Kazarinov, R. A. Suris, *Sov. Phys. Semicond.* **5**, 797 (1971).

[2] J. Faist, F. Capasso, D. L. Sivco, C. Sirtori, A. L. Hutchinson, and A. Y. Cho, *Science* **264**, 553 (1994).

[3] C. Gmachl, F. Capasso, D. L. Sivco, and A. Y. Cho, *Rep. Prog. Phys.* **64**, 1533 (2001).

[4] F. Capasso, C. Gmachl, R. Paiella, A. Tredicucci, A. L. Hutchinson, D. L. Sivco, J. N. Baillargeon, A. Y. Cho, and H. C. Liu, *IEEE J. Sel. Top. Quantum Electron*. **6**, 931 (2000).

[5] B. S. Williams, *Nature Photonics* **1**, 517 (2007)

[6] C. Sirtori, S. Dhillon, C. Faugeras, A. Vasanelli, and X. Marcadet, *Physica Status Solidi A* **203**, 3533 (2006).

[7] C.Sirtori, P. Kruck, S. Barbieri, P. Collot, J. Nagle, M. Beck, J. Faist, and U. Oesterle, *Appl. Phys. Lett.* **73**, 3486–8 (1998)

[8] G. Dehlinger, L. Diehl, U. Gennser, H. Sigg, J. Faist, K. Ensslin, D. Grutzmacher, and E. Muller, *Science* **290**, 2277 (2000).

[9] J. Faist, F. Capasso, C. Sirtori, D. L. Sivco, J. N. Baillargeon, A. L. Hutchinson, S.-N. G. Chu, and A. Y. Cho, *Appl. Phys. Lett.* **68** 3680 (1996).

[10] J. Faist, F. Capasso, C. Sirtori, K. West, and L. N. Pfeiffer, *Nature* **387**, 777 (1997).

[11] G. Scamarcio, F. Capasso, C. Sirtori, J. Faist, A. L. Hutchinson, D. L. Sivco and A. Y. Cho, *Science* **276**, 773 (1997).

[12] F. Capasso, *Optical Engineering* 49, 111102 (2010).

[13] H. Page, C. Becker, A. Robertson, G. Glastre, V. Ortiz, and C. Sirtori, *Appl. Phys. Lett.* **78**, 3529 (2001).

[14] J. C. Shin, M. D'Souza, Z. Liu, J. Kirch, L. J. Mawst, D. Botez, I. Vurgaftman, and J. R. Meyer, *Appl. Phys. Lett.* **94**, 201103 (2009).

[15] S. L. Chuang, *Physics of Optoelectronic Devices* (Wiley Interscience, New York, 1995).

[16] J. M. Luttinger and W. Kohn, *Phys. Rev.* **97**, 869 (1955).

[17] G. L. Bir and G. E. Pikus, *Symmetry and Strain-Induced Effects in Semiconductors* (Wiley, New York, 1974).

[18] L. R. Ram-Mohan, K. H. Yoo, and R. L. Aggarwal, *Phys. Rev. B* **38**, 6151 (1988).

[19] G. Liu and S. L. Chuang, *Phys. Rev. B* **65**, 165220 (2002).

[20] E. O. Kane, *Semiconductors and Semimetals*, vol. 1 (Academic, New York, 1966).

[21] C. R. Pidgeon and R. N. Brown, *Phys. Rev.* **146**, 575 (1966).

[22] I. Vurgaftman and J. R. Meyer, *J. Appl. Phys.* **89**, 5815 (2001).

[23] S. Barbieri, F. Beltram, and F. Rossi, *Phys. Rev. B* **60**, 1953 (1999).

[24] B. Vinter, *Phys. Rev. B* **66**, 045324 (2002).

[25] M. A. Stroscio and M. Dutta, *Phonons in Nanostructures* (Cambridge University Press, 2001).

[26] B. K. Ridley, *Electrons and Phonons in Semiconductor Multilayers* (Cambridge University Press, 1997).

[27] M. Babiker, *J. Phys. C: Solid St. Phys.* **19**, 683 (1986).

[28] H. R ¨ucker, E. Molinari, and P. Lugli, *Phys. Rev. B* **45**, 6747 (1992).

[29] X. Gao, D. Botez, and I. Knezevic, *J. Appl. Phys.* **103**, 073101 (2008).

[30] X. Gao, D. Botez, and I. Knezevic, *J. Comput. Electron.* **7**, 209 (2008).

[31] S. M. Goodnick and P. Lugli, *Hot Carriers in Semiconductor Nanostructures* (Academic, New York, 1992).

[32] C. Jacoboni and P. Lugli, *The Monte Carlo Method for Semiconductor Device Simulation* (Springer-Verlag, New York, 1989).

[33] O. E. Raichev, *Phys. Rev. B* **49**, 5448 (1994).

[34] S. Borenstain and J. Katz, *Phys. Rev. B* **39**, 10852 (1989).

[35] B. S. Williams, Ph.D. thesis, Massachusetts Institute of Technology, 2003.

[36] X. Gao, Ph.D. thesis, University of Wisconsin-Madison, 2008.

[37] S. M. Goodnick and P. Lugli, *Phys. Rev. B* **37**, 2578 (1988).

[38] M. Mosko and A. Moskova, *Phys. Rev. B* **44**, 10794 (1991).

[39] M. Lundstrom, Fundamentals of Carrier Transport (University Press, Cambridge, 2000).

[40] R. C. Iotti and F. Rossi, *Phys. Rev. Lett.* **87**, 146603 (2001).

[41] C. jacoboni and L. Reggiani, *Rev. Mod. Phys.* **55**, 645 (1983).

[42] K. Tomizawa, *Numerical Simulation of Submicron Semiconductor Devices*

(Artech House, Boston, 1993).

[43] X. Gao, D. Botez, and I. Knezevic, *Appl. Phys. Lett.* **89**, 191119 (2006).

[44] X. Gao, D. Botez, and I. Knezevic, *J. Appl. Phys.* **101**, 063101 (2007).

[45] R. C. Iotti and F. Rossi, Appl. Phys. Lett. 78, 2902 (2001).